scientific reports

Check for updates

OPEN

Isoprenoid-chained lipid EROCOC$_{17+4}$: a new matrix for membrane protein crystallization and a crystal delivery medium in serial femtosecond crystallography

Kentaro Ihara[1,7], Masakatsu Hato[1,7]✉, Takanori Nakane[2,6], Keitaro Yamashita[2,3], Tomomi Kimura-Someya[1], Toshiaki Hosaka[1], Yoshiko Ishizuka-Katsura[1], Rie Tanaka[3,4], Tomoyuki Tanaka[3,4], Michihiro Sugahara[3,4], Kunio Hirata[3], Masaki Yamamoto[3], Osamu Nureki[2], Kensuke Tono[3,5], Eriko Nango[3,4], So Iwata[3,4] & Mikako Shirouzu[1]✉

In meso crystallization of membrane proteins relies on the use of lipids capable of forming a lipidic cubic phase (LCP). However, almost all previous crystallization trials have used monoacylglycerols, with 1-(*cis*-9-octadecanoyl)-*rac*-glycerol (MO) being the most widely used lipid. We now report that EROCOC$_{17+4}$ mixed with 10% (w/w) cholesterol (Fig. 1) serves as a new matrix for crystallization and a crystal delivery medium in the serial femtosecond crystallography of Adenosine A$_{2A}$ receptor (A$_{2A}$R). The structures of EROCOC$_{17+4}$-matrix grown A$_{2A}$R crystals were determined at 2.0 Å resolution by serial synchrotron rotation crystallography at a cryogenic temperature, and at 1.8 Å by LCP-serial femtosecond crystallography, using an X-ray free-electron laser at 4 and 20 °C sample temperatures, and are comparable to the structure of the MO-matrix grown A$_{2A}$R crystal (PDB ID: 4EIY). Moreover, X-ray scattering measurements indicated that the EROCOC$_{17+4}$/water system did not form the crystalline L$_C$ phase at least down to − 20 °C, in marked contrast to the equilibrium MO/water system, which transforms into the crystalline L$_C$ phase below about 17 °C. As the L$_C$ phase formation within the LCP-matrix causes difficulties in protein crystallography experiments in meso, this feature of EROCOC$_{17+4}$ will expand the utility of the in meso method.

In meso crystallization of membrane proteins (MPs), a powerful technique for MP structure determination, critically relies on the choice of the lipids that form the LCP around room temperature[1,2]. In the method, a solubilized target MP is homogenized with an LCP-forming lipid, to uniformly reconstitute the MP into the native biomembrane mimetic LCP lipid bilayer. The added crystallization solution triggers the nucleation and crystal growth of the MP within the lipid bilayer environment, where the crystallization process essentially relies on the three-dimensional bi-continuous LCP bilayer architecture[2]. Moreover, the recent development of viscous media injectors[3] has facilitated the direct use of a native crystal growth LCP-matrix as a crystal delivery medium in serial femtosecond or millisecond crystallography (SFX or SMX), known as LCP-SFX and LCP-SMX, respectively[4,5].

[1]RIKEN Center for Biosystems Dynamics Research, 1-7-22 Suehiro-cho, Tsurumi-ku, Yokohama, Kanagawa 230-0045, Japan. [2]Department of Biological Sciences, Graduate School of Science, The University of Tokyo, 7-3-1 Hongo, Bunkyo-ku, Tokyo, Japan. [3]RIKEN SPring-8 Center, 1-1-1, Kouto, Sayo-cho, Sayo-gun, Hyogo 679-5148, Japan. [4]Department of Cell Biology, Graduate School of Medicine, Kyoto University, Yoshidakonoe-cho, Sakyo-ku, Kyoto 606-8501, Japan. [5]Japan Synchrotron Radiation Research Institute, 1-1-1, Kouto, Sayo-cho, Sayo-gun, Hyogo 679-5198, Japan. [6]Present address: MRC Laboratory of Molecular Biology, Cambridge Biomedical Campus, Francis Crick Ave, Cambridge CB2 0QH, UK. [7]These authors contributed equally: Kentaro Ihara and Masakatsu Hato. ✉email: masakatsu.hato@alum.riken.jp; mikako.shirouzu@riken.jp

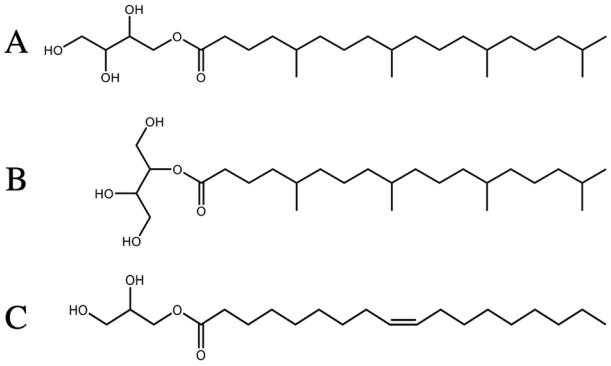

Figure 1. Chemical structure of 1-*O*-(5, 9, 13, 17-tetramethyloctadecanoyl)-*rac*-erythritol (**A**) and 2-*O*-(5, 9, 13, 17-tetramethyloctadecanoyl)-*rac*-erythritol (**B**). The lipid used in this study was a mixture of 92% 1-*O*- and 8% 2-*O*-isomers, which is abbreviated to $EROCOC_{17+4}$. In the $A_{2A}R$ crystallization trials, a 9:1 (w/w) mixture of $EROCOC_{17+4}$ and cholesterol was employed as a crystallization matrix, which is referred to as an $EROCOC_{17+4}$-matrix (see Methods Crystallization section for more details). The isoprenoid chain is abbreviated as C_{p+q}, where p and q stand for the number of carbon atoms in the longest unbranched carbon chain in the molecule (excluding the carbonyl carbon) and the number of methyl branches along it, respectively. Thus, $EROCOC_{17+4}$ represents a lipid molecule, in which the C_{17+4} chain is linked to the erythritol head group (ER) via an ester linkage (OCO). (**C**) Chemical structure of 1-(*cis*-9-octadecanoyl)-*rac*-glycerol (MO). It is noted that $EROCOC_{17+4}$ and MO both possess the acyl chain of 18 carbon atoms-long.

In spite of the increasing functional roles of the LCP, the currently available lipid species have been restricted by the limited choice of polar lipids. In fact, almost all of the past crystallization trials and LCP-SFX data collections have been performed by using monoacylglycerols (MAGs) at room temperature, with MO being the most widely used lipid[6]. However, MO is not ideal. For instance, according to the equilibrium phase diagram of the MO/water system, the MO-LCP gives way to the L_C phase below about 17 °C[7]. As LCP is prone to supercooling[8], the MO-LCP may remain supercooled below 17 °C. However, as the MO-LCP is metastable below 17 °C, the risk always remains that the LCP → L_C phase transition could occur at any time during the experiment. The LCP → L_C phase transition incurs numerous difficulties. For example, the L_C phase does not support MP crystallization, and in LCP-SFX, when microcrystals randomly dispersed in the MO-LCP are injected into an evacuated X-ray diffraction chamber at 20 °C, evaporative cooling causes transformation into the MO-L_C phase. This leads to strong MO-L_C Bragg diffractions from crystallized hydrocarbon chains and three-dimensional orders in the L_C molecular packing, which interfere with the diffraction spots from MP crystals[3]. As background reduction is crucial in serial microcrystallography[9], there is a need to develop new lipid matrices that support MP crystallization and do not undergo the LCP → L_C phase transition in LCP-SFX[4]. We now report that one of the LCP-forming isoprenoid-chained lipids (IPCLs), $EROCOC_{17+4}$ with the acyl chain of 18 carbon atoms-long[10,11] (see Fig. 1 for more details), serves as a new matrix lipid that satisfies the above requirements.

The recently developed LCP-forming IPCLs[10–14], are characterized by their regularly methyl-branched chain structure (oligomers of a $-(CH_2)_2CHCH_3CH_2-$ unit with a terminal $-(CH_2)_2CHCH_3CH_3$ unit, see Fig. 1), which is remarkably different from that of MAGs, consisting of different lengths of linear hydrocarbon chains with a *cis*-double bond at various chain positions (see Fig. 1)[6]. Owing to the regularly branched chain structure, IPCL-LCPs are characterized by the low L_C → LCP phase transition temperature (T_K): most of the T_K values are close to or below 0 °C, as shown in Supplementary Table 1[10–14]. Thus, they are attractive as a new crystallization matrix lipid for temperature-sensitive proteins and as an L_C phase formation-free crystal delivery medium in LCP-SFX. However, to the best of our knowledge, only two structural analyses of bacteriorhodopsin (bR) with IPCL-matrices have been reported so far. One used an ether-type β-$XylOC_{16+4}$[13], which yielded crystals at 2 Å resolution with a reduced crystallographic twin ratio[15], and the other used an amide-type $GlyNCOC_{15+4}$, where the successful crystallization was performed at both 20 and 4 °C[12]. However, the utility of IPCLs as a possible crystal delivery medium in LCP-SFX has not been evaluated.

To assess $EROCOC_{17+4}$ as a possible matrix lipid for MP crystallization and a crystal delivery medium in LCP-SFX, we employed the G protein-coupled receptor $A_{2A}R$ as a model MP, considering that MO-matrix, a 9:1 (w/w) mixture of MO and cholesterol, grown high-resolution crystal structures with ordered lipids have been reported[16–19]. We now demonstrate that $EROCOC_{17+4}$-matrix, a 9:1 (w/w) mixture of $EROCOC_{17+4}$ and cholesterol (see Methods Crystallization section for more details), supports the crystallization of $A_{2A}R$ at 20 °C, yielding a high-resolution crystal structure comparable to that of the MO-matrix grown crystals at 1.8 Å resolution (PDB ID: 4EIY, hereafter referred to as the 4EIY model), and that $EROCOC_{17+4}$-matrix allows us to perform the LCP-SFX data collection with a sample kept at 4 °C, without the L_C phase formation.

Results and discussion

Crystallization of $A_{2A}R$ in the $EROCOC_{17+4}$-matrix. In the screening of crystallization conditions of $A_{2A}R$ as a model MP with the $EROCOC_{17+4}$-matrix, we first noted that the optimal crystallization conditions for the MO-matrix, i.e., 100 mM sodium citrate, pH 5.0, 25–28% PEG400, 40–60 mM NaSCN, and 2% 2,5-hexan-

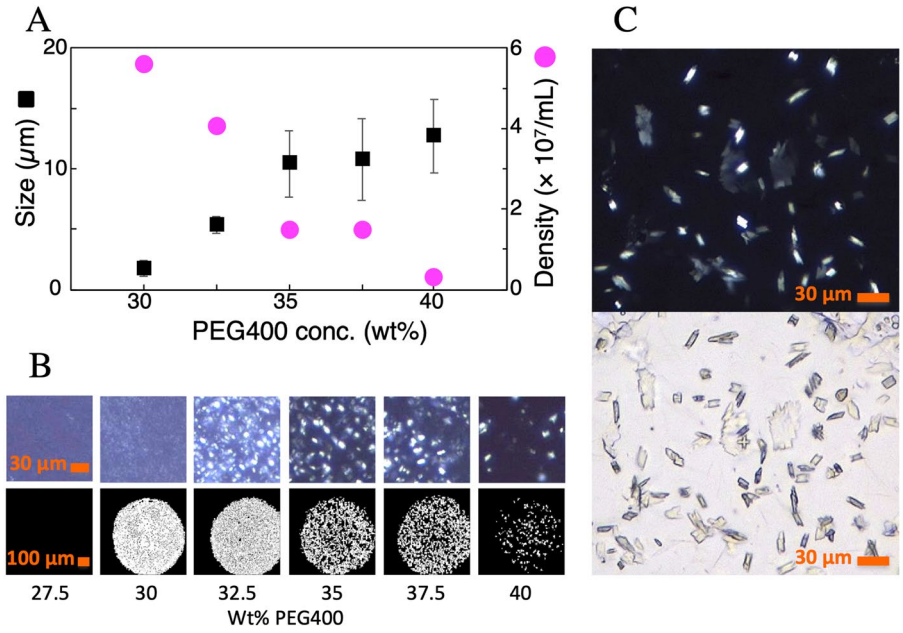

Figure 2. Effect of PEG concentration on size and density of $A_{2A}R$ crystals grown in the $EROCOC_{17+4}$-matrix. (**A**) Size (black) and density (magenta) of $EROCOC_{17+4}$-matrix grown $A_{2A}R$ crystals as a function of the PEG400 concentration, in an otherwise fixed solution composed of 50 mM NaSCN, 2% 2,5-hexanediol, and 100 mM Na citrate, pH 5.50. (**B**) Cross polarized (upper) and second harmonic generation (lower) images in a 96-well glass screening plate, showing the birefringence and chirality-derived signals of the protein crystals, respectively. (**C**) Crystals used for SS-ROX under optimized conditions: 38% PEG400, 50 mM NaSCN, 2% 2,5-hexanediol, and 100 mM Na citrate, pH 5.75. Upper: cross polarized, lower: bright field.

ediol[16], supported micro-crystal (≤ ~ 1 μm) formation in the $EROCOC_{17+4}$-matrix at 20 °C. However, these crystals were too small for high-resolution structural analyses. To identify the optimum crystallizing conditions for the $EROCOC_{17+4}$-matrix, we screened the effects of the pH (4.5–6.5 with 25–300 mM sodium citrate), and the concentrations of PEG400 or PEG300 (17.5–47.5%), NaCl (0–1000 mM), and the additives NaSCN (0–60 mM) and 2,5-hexanediol (0–2%), on the crystallization behavior, and noted that the most effective parameter was the PEG400 (or equivalently PEG300) concentration. The size and density of $EROCOC_{17+4}$-matrix grown $A_{2A}R$ crystals as a function of the PEG400 concentration (C_{PEG400}), in an otherwise fixed solution composition of 50 mM NaSCN, 2% 2,5-hexanediol, and 100 mM Na citrate, pH 5.50, are shown in Fig. 2A,B

The crystal size tended to increase as C_{PEG400} increased; 3–10 μm at 30–35%, and eventually reaching ~ 15 μm sized-crystals at 35–40% PEG400, where the first crystals appeared at 1–2 days and continued to grow over ~ 1 week to reach the maximum size of ~ 25 μm (Fig. 2C), which is suitable for data collection by serial synchrotron rotation crystallography (SS-ROX)[20].

On the other hand, the crystal density decreased as C_{PEG400} increased, from 10^7–10^8 crystals/mL around 30% down to 10^6–10^7 crystals/mL around 40%. The C_{PEG400}-dependent crystal size/density relation shown in Fig. 2A served as a useful guide for preparing ~ 50 μL of LCP densely packed with small crystals (≥ 10^7 crystals/mL and 5–10 μm) needed for complete data collection by LCP-SFX. The final crystallization condition for the $EROCOC_{17+4}$-matrix based LCP-SFX was 100 mM sodium citrate, pH 5.5, 37% PEG300, 50 mM NaSCN, and 2% 2,5-hexanediol. Thus, except for the PEG concentrations, the optimum crystallization conditions for $A_{2A}R$ in the $EROCOC_{17+4}$-matrix did not differ significantly from those for the MO-matrix: the $EROCOC_{17+4}$-matrix required 35–40% PEG400/PEG300, as compared to 25–28% PEG400 for the MO-matrix.

Crystallographic analyses by SS-ROX and LCP-SFX. The crystallographic data of the $EROCOC_{17+4}$-matrix grown $A_{2A}R$ crystals are summarized in Table 1. In the present SS-ROX and LCP-SFX experiments, we employed the $A_{2A}R$ crystals prepared at 20 °C. The samples for SS-ROX were flash frozen in SS-ROX_cryo, and those for the LCP-SFX loaded into the injector were kept at 4 or 20 °C during the measurements in LCP-SFX_4 °C and LCP-SFX_20 °C, respectively. The crystallographic space group of these $EROCOC_{17+4}$-matrix grown crystals was the same as that for the MO-matrix grown crystals (PDB ID 4EIY), $C222_1$. The structures of the $EROCOC_{17+4}$-matrix grown $A_{2A}R$ crystals were determined at 2.0 Å resolution by SS-ROX at the cryogenic temperature, and at 1.8 Å by LCP-SFX_4 °C and LCP-SFX_20 °C, respectively. As in the cases described in the references[21,22], no significant differences were observed in the electron density maps and the models obtained at the three temperatures, except for the increasing *B* factors and the decreasing number of water molecules at the higher temperatures (Table 1). The resolution of the LCP-SFX data was slightly better than that of the SS-ROX data for the present measurements, although the LCP-SFX and SS-ROX data are difficult to compare because the crystals and X-ray sources are different. On the other hand, comparing the LCP-SFX_4 °C and LCP-SFX_20 °C data obtained under exactly the same conditions, except for the sample

Data	LCP-SFX_20 °C	LCP-SFX_4 °C	SS-ROX_cryo
Sample temperatures (K)	293	277	100
PDB ID	6LPK	6LPJ	6LPL
Data collection			
Beamline	SACLA, BL3	SACLA, BL3	SPring-8, BL32XU
Wavelength (Å)	1.230	1.230	1.000
Crystal size (μm)	5–10	5–10	~15
Number of collected images	169,712	143,099	50,668
Number of hit images	34,216	65,791	6346
Number of indexed images	31,312	46,877	3701
Number of merged images	31,312	46,877	2100
Crystal hit rate (%)[a]	20.2	46.0	12.5
% indexed images (%)[b]	18.5	32.8	7.3
Crystal index rate (%)[c]	91.5	71.3	58.3
Cell constants a, b, c (Å)	40.5, 179.2, 142.9	40.4, 178.9, 142.4	39.9, 179.3, 141.0
Space group	$C222_1$	$C222_1$	$C222_1$
Processed resolution (Å)	30.4–1.80 (1.83–1.80)	30.3–1.80 (1.83–1.80)	42.8–2.00 (2.08–2.00)
R_{split} (%)	7.1 (107.9)	6.6 (99.4)	9.0 (63.8)
$CC_{1/2}$ (%)	99.5 (39.3)	99.6 (39.3)	99.1 (47.2)
Total measurements	14,994,871 (221,521)	16,847,719 (236,481)	1,729,208 (193,264)
Unique reflections	48,924 (2,438)	48,530 (2,390)	34,815 (3,765)
Completeness (%)	100 (100)	100 (100)	100 (100)
Multiplicity	306.5 (90.9)	344.7 (98.9)	49.7 (51.6)
SNR or averaged I/σ(I)	7.6 (1.0)	8.3 (1.1)	7.3 (1.9)
Wilson B value ($Å^2$)	35.0	32.4	34.2
Refinement			
R_{work} (%)	17.7 (34.6)	17.5 (33.9)	17.3 (26.4)
R_{free} (%)	20.9 (35.8)	20.7 (35.7)	20.8 (24.2)
R.m.s. bond lengths (Å)	0.011	0.011	0.011
R.m.s. bond angles (°)	1.58	1.55	1.68
Overall B value ($Å^2$):	56.2	51.8	49.0
B for A_{2A}R-bRIL ($Å^2$)	53.2	49.1	46.7
B for A_{2A}R ($Å^2$)	43.5	40.1	38.3
B for bRIL ($Å^2$)	84.6	78.6	74.2
B for ZM241385 ($Å^2$)	33.1	30.3	29.4
B for Na^+ ($Å^2$)	31.5	28.7	35.1
B for cholesterol ($Å^2$)	55.5	50.2	48.0
B for $EROCOC_{17+4}$ ($Å^2$)	85.4	77.1	73.7
B for hydrocarbons ($Å^2$)	85.7	79.1	71.9
B for water ($Å^2$)	58.3	54.1	50.5
Number of amino acids in A_{2A}R	299	299	299
Number of amino acids in bRIL	91	91	91
Number of ZM241385	1	1	1
Number of Na^+	1	1	1
Number of cholesterol	3	3	3
Number of $EROCOC_{17+4}$	2	2	2
Number of hydrocarbons	20	20	20
Number of water	116	123	138
Ramachandran favored	383 (99.2%)	384 (99.5%)	380 (98.4%)
Ramachandran allowed	3 (0.8%)	2 (0.5%)	6 (1.6%)
Ramachandran outlier	0 (0.0%)	0 (0.0%)	0 (0.0%)

Table 1. Data collection and refinement statistics at three sample temperatures. [a](Number of hit images/Number of collected images) × 100. [b](Number of indexed images/Number of collected images) × 100. [c](Number of indexed images/Number of hit images) × 100.

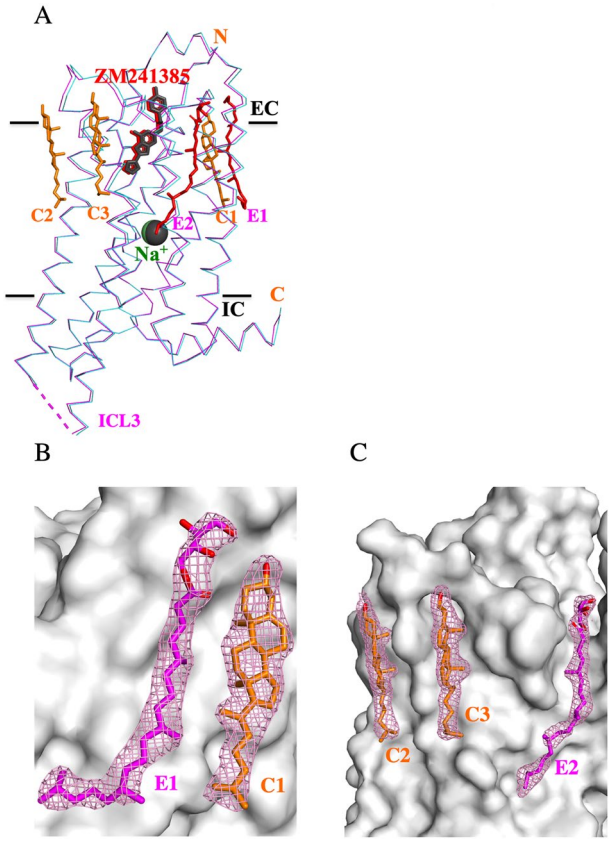

Figure 3. Comparison of $EROCOC_{17+4}$- and MO-matrix grown $A_{2A}R$ crystal structures. (**A**) Crystal structures of LCP-SFX_4 °C (magenta) and 4EIY (cyan). The bRIL moiety inserted in ICL3 is omitted from the coordinates (magenta dashes). Sodium ions (green and dark grey balls for LCP-SFX_4 °C and 4EIY, respectively) and ZM241385 (red and dark grey sticks for LCP-SFX_4 °C and 4EIY, respectively) are also shown. Black lines approximately correspond to the hydrophobic/hydrophilic boundary of the lipid bilayer. IC and EC are intracellular and extracellular sides, respectively. Two well characterized $EROCOC_{17+4}$ (red; E1 and E2) and three cholesterol (orange; C1, C2 and C3) models are displayed as sticks. (**B**,**C**) Molecular surface of LCP-SFX_4 °C with well characterized lipids. The $2mF_o$-DF_c electron density maps around the lipid models are contoured at 1.0 σ (pink mesh). The carbon atoms of the $EROCOC_{17+4}$ and cholesterol stick models are shown in magenta and orange, respectively. The oxygen atoms of both lipids are shown in red. This figure is prepared by PyMOL Ver. 1.8 (https://pymol.org).

temperatures, the LCP-SFX_4 °C model seems to be more reliable. The reliability factors, signal-to-noise ratio (SNR) values, and average *B* values for LCP-SFX_4 °C are slightly better than those for LCP-SFX_20 °C (Table 1). For example, the $R_{split/work/free}$ values for LCP-SFX_4 °C are 6.6/17.5/20.7% whereas those of LCP-SFX_20 °C are 7.1/17.7/20.9%. Since the diffraction data could be improved by lowering the sample temperature, as described above, the LCP-SFX_4 °C model is used for further structure comparisons and analyses. The root mean square deviation (RMSD) value for the corresponding 299 Cα atoms between the LCP-SFX_4 °C and the MO-matrix based 4EIY model is 0.23 Å RMSD, and those for the inter Na^+, a conserved sodium ion bound in $A_{2A}R$, and ZM241385, a strong inverse agonist for $A_{2A}R$, are 0.20 and 0.18 Å, respectively (Fig. 3A).

Lipid molecules on the $A_{2A}R$ surface. After the refinement of the $A_{2A}R$ structure, the electron density maps showed elongated extra electron densities surrounding the protein, which are usually assigned to lipid molecules. The locations of the extra electron densities observed in this work did not significantly depend on the sample temperatures. Moreover, the positions of the extra electron densities on the present $A_{2A}R$ surface nearly overlapped with those of the electron densities corresponding to lipids in the MO-matrix based 4EIY model, suggesting that the lipid binding positions remain nearly unaltered in the two different matrix lipid environments.

Although the majority of the extra electron densities are rather obscure, we noted that five extra electron densities on the extracellular half of the $A_{2A}R$ surface can be assigned to two different lipid species, cholesterol and $EROCOC_{17+4}$. The cholesterols are probably derived from the LCP crystallization matrix, whereas the possibility that it is derived from insect cell membrane cannot be ruled out. As shown in Fig. 3A, there are three cholesterol molecules, C1, C2, and C3, at the same locations as those of the three cholesterol molecules identified in the 4EIY model. Two $EROCOC_{17+4}$ molecules, E1 and E2, are also depicted in Fig. 3A.

XFEL beam	d/μm	$D_{4\,°C}/D_{20\,°C}$	$D_{4\,°C}$/μm[a]	$D_{20\,°C}$/μm[a]
Off	75	1.3	94 ± 3 (10)	75 ± 3 (12)
ON	75	1.8	135 ± 56 (65)	73 ± 20 (26)

Table 2. The LCP stream diameter ratio $D_{4\,°C}/D_{20\,°C}$ in the absence and presence of the XFEL beam. d: Injector nozzle diameter, $D_{4\,°C}$, $D_{20\,°C}$: LCP stream diameters at 4 and 20 °C. [a]Individual $D_{4\,°C}$, $D_{20\,°C}$ and standard deviation values, which were estimated by assuming that the average LCP stream diameter at 20 °C in the absence of the XFEL beam was equal to the injector nozzle diameter d; i.e., $D_{20\,°C}$ (beam off)$_{average} \equiv 75$ μm. The number of LCP stream diameter measurements performed every second is shown in parentheses.

The electron density for E1, which is located near cholesterol C1, is well defined for the full EROCOC$_{17+4}$ molecule: an isoprenoid chain with four methyl branches at the 5th, 9th, 13th, and 17th carbons and a hydrophilic erythritol connected via an ester bond (Fig. 3B and Sup. Figure 1A). Since IPCLs are not native lipids in the insect cells where the $A_{2A}R$ proteins were produced, the electron density for E1 can be unambiguously modeled as EROCOC$_{17+4}$. Another EROCOC$_{17+4}$ modeled with relatively clear electron densities for the methyl branches (E2 in Fig. 3A,C and Sup. Figure 1B) exists between helices I and VII. E2 may stabilize the N-terminal segment of helix I, as proposed for the corresponding lipid (OLA11) in the 4EIY model[16]. It is interesting that this lipid binding site corresponds to the antagonist/ligand binding site of the prostaglandin E receptor EP_4, which may be on the ligand entry pathway[23]. In the 4EIY model, the lipids corresponding to E1 and E2 are MO and oleic acid, respectively. The electron densities for the three terminal carbons of the MO and the two terminal carbons of the oleic acid are weak, possibly due to the flexibility of the terminal regions of the oleic lipids.

LCP-SFX data collection at 4 and 20 °C sample temperatures. As described in the preceding section, the reliability factors of the data were improved by lowering the sample temperature. Table 1 also shows that the LCP-SFX data collection statistics depended on the sample temperature. For instance, the "crystal hit rate" (*Number of hit images/Number of collected images*) × 100 was as high as 46.0% for the LCP-SFX_4 °C, while it dropped to 20.2% for the LCP-SFX_20 °C, where the *hit image* is defined as an image with 20 or more diffraction spots, among all images collected at a 30 Hz frequency. The "% indexed images" (*Number of indexed images/Number of collected images*) × 100[4] likewise displayed a similar trend, 32.8% and 18.5% for the LCP-SFX_4 °C and the LCP-SFX_20 °C, respectively. As the present LCP-SFX experiments were performed with the identical $A_{2A}R$ crystal-dispersed LCP, and except for the sample temperatures, were performed under the identical LCP-SFX experimental conditions (e.g., the injector nozzle diameter, the XFEL beam size, the pulse intensity, etc.), these results were most presumably ascribable to the different sample temperatures.

Table 2 lists the $D_{4\,°C}/D_{20\,°C}$ ratios estimated from the real-time LCP stream images, in the absence and presence of the XFEL beam, where $D_{4\,°C}$ and $D_{20\,°C}$ stand for the EROCOC$_{17+4}$-LCP stream diameters at 4 and 20 °C at the XFEL beam intersection position, respectively. For reference, individual values of $D_{4\,°C}$ and $D_{20\,°C}$, are also listed. These values were estimated by assuming that the average LCP stream diameter at 20 °C in the absence of the XFEL beam was equal to the injector nozzle diameter d; i.e., $D_{20\,°C}$ (beam off)$_{average} \equiv 75$ μm. It is first noted that the ratio in the absence of the beam, $D_{4\,°C}$ (beam off)/$D_{4\,°C}$ (beam off) ≈1.3. This suggests that the rheological properties of the EROCOC$_{17+4}$-LCP are temperature dependent. In fact, we noted that the EROCOC$_{17+4}$-LCP stream at 20 °C displayed "viscous fluid-like" behavior, whereas at 4 °C, "stiff or solid-like" features became conspicuous. This appears consistent with our empirical observation that the stress required to homogenize the EROCOC$_{17+4}$-LCP progressively increases as the temperature is lowered. Moreover, the ratio in the presence of the beam, $D_{4\,°C}$ (beam on)/$D_{20\,°C}$ (beam on) ≈ 1.8, predicts that the "crystal hit rate" at 4 °C will be doubled as compared to that at 20 °C, in line with the observed "crystal hit rate". This ratio also predicts the increased probability of multiple hits at 4 °C. The data in support of this prediction are actually seen in the "crystal index rate" (*Number of indexed images/Number of hit images*) × 100, with values of 71.3% at 4 °C and 91.5% at 20 °C.

Although the LCP stream was smooth and continuous in the absence of the XFEL beam, the beam-LCP stream intersection caused the LCP stream to exhibit quite dynamic and temperature-dependent behaviors in the presence of the XFEL beam. At 20 °C, the "viscous fluid-like" LCP stream displayed frequent fission and blowing-off of the stream at regular intervals, without significantly altering the $D_{20\,°C}$ (beam on) as compared to $D_{20\,°C}$ (beam off). On the other hand, at 4 °C the fission/blowing-off frequency of the "stiff or solid-like" LCP stream was reduced and occurred less regularly, tending to form an LCP lump with a larger $D_{4\,°C}$ (beam on) as compared to $D_{4\,°C}$ (beam off). Thus, the temperature-dependent LCP-SFX data collection statistics were most presumably ascribable to the modified response of the "viscous fluid-like" versus the "stiff or solid-like" LCP stream to the beam intersection.

To summarize, the LCP-SFX data collection at the 4 °C sample temperature could be performed with the higher "% indexed images" (32.8%) as compared to that at the 20 °C sample temperature (18.5%), and yielded more reliable diffraction data. The signal-to-noise ratio was also improved for the LCP-SFX_4 °C as compared to that for the LCP-SFX_20 °C; i.e., 8.3 and 7.6 at 4 and 20 °C, respectively, suggesting that the enhanced signal at 4 °C outweighed the presumed increase in the lipid-derived background diffraction from the LCP-stream with an increased D value. Therefore, the use of low temperature LCP samples could be a useful option for the LCP-SFX data collection.

EROCOC$_{17+4}$ and the EROCOC$_{17+4}$-matrix are resistant to adopting the crystalline L_C phase. Lipid/water systems generally exhibit a transition from a high temperature liquid crystalline to a low temperature

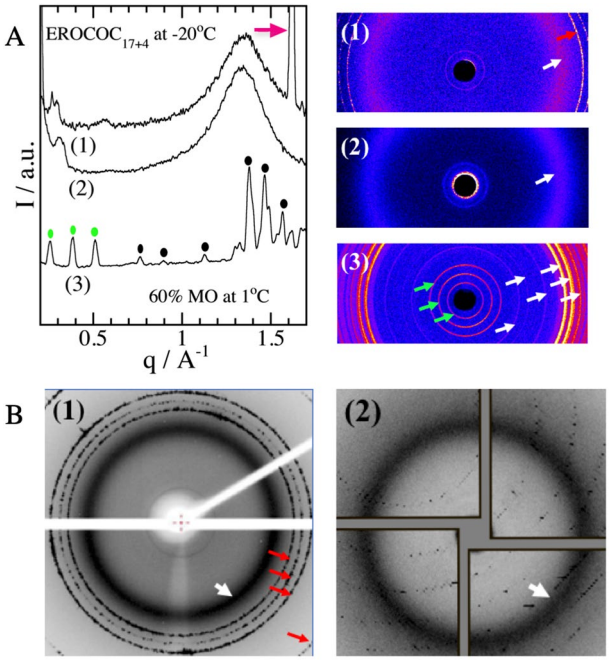

Figure 4. (**A**) X-ray diffraction profiles of 62.5% (w/w) $EROCOC_{17+4}$/water (1) and dry $EROCOC_{17+4}$ (2) at − 20 °C, together with the 2D-diffraction images used to construct each diffraction profile. The white and red arrows denote diffractions from disordered chains on the lipid and from ice, respectively. Profile (3) is from the MO-L_C phase [60% (w/w) MO/water] at 1 °C. The humps observed in profiles (1) and (2) below q ~ 0.35 $Å^{-1}$ are due to x-ray leaks around the beam stopper. $q = (4\pi sin\theta)/\lambda$, where 2θ is the scattering angle and the wavelength λ = 1.54 Å. (**B**) (1) A diffraction image of the $EROCOC_{17+4}$-matrix, 60% 9:1 (w/w) $EROCOC_{17+4}$/cholesterol/water, at − 180 °C (measured under an evaporated liquid nitrogen flow). The broad band around 4.6 Å (white arrow) indicates that $EROCOC_{17+4}$ remained in a disordered chain state at − 180 °C. The four red arrows denote hexagonal ice diffractions. (2) A diffraction image from the $A_{2A}R$ crystallization $EROCOC_{17+4}$-matrix during the LCP-SFX_4°C data collection in a helium gas environment.

crystalline L_C phase at a lipid-specific temperature, T_K. Above T_K, the lipid chains are in a fluid-like disordered conformation (a disordered chain state), with X-ray diffraction profiles characterized by a broad band around 4.6 Å, similar to a band observed from liquid paraffines[24]. Below T_K, the lipid adopts a crystalline L_C phase, where the chains are fully extended and aligned parallel to each other, which is characterized by multiple sharp diffractions at all spacings from the small angle X-ray scattering (SAXS) to wide angle X-ray scattering (WAXS) regimes, reflecting the presence of long- and short-range three-dimensional orders in the molecular packing[24].

A typical example of an X-ray diffraction profile from an L_C phase is shown in Fig. 4A-(3), where the profile from the 60% (w/w) MO/water system at 1 °C is plotted. Note that the equilibrium MO/water system adopts the crystalline L_C phase below 17 °C[7]. Six representative peaks in the larger q region are denoted by black dots in the profile and white arrows in the 2D image. The three sharp diffractions in the SAXS regime, denoted by the green dots in the profile and green arrows in the 2D-image in Fig. 4A-(3), are due to the 2nd, 3rd, and 4th diffractions of the MO-L_C phase with a lattice constant of 49.6 Å, which reasonably agrees with the reported value of 49.2 Å[25].

Before discussing the phase behavior of the $EROCOC_{17+4}$/water system at − 20 and around − 40 ~ to − 60 °C, let us briefly outline the phase behavior of the $EROCOC_{17+4}$/water system above 0 °C[10]. The $EROCOC_{17+4}$-LCP is identified in the lipid concentration $W_{Lipid}(= 100 - W_{Water})$ range from 60 to 80% (w/w) and over a temperature range from ca. 0 to ca. 55 °C [10, Sup. Table 1]. Thus, W_{Lipid} = 60% (w/w) represents the water saturated $EROCOC_{17+4}$-LCP composition. Once W_{Lipid} is decreased below 60% (w/w), the excess water that can no longer be incorporated within the LCP separates out to adopt the "excess water + water saturated LCP" two-phase coexisting state. In the W_{Lipid} range from 80 to ca. 92% (w/w), the system adopts a lamellar (L_α) phase. In the highest W_{Lipid} regime above ca. 93% (w/w), the phase structures have not yet been identified, due to the slow rate toward reaching the equilibrium state.

The X-ray diffraction profiles from the 62.5% (w/w) $EROCOC_{17+4}$/water and dry $EROCOC_{17+4}$ at − 20 °C are shown in Fig. 4A-(1) and (2), respectively. Both profiles are quite distinct from that of the MO-L_C phase in Fig. 4A-(3). They are characterized by a broad band around 4.7 Å, [$q(\equiv 2\pi/d)$ ~1.3 $Å^{-1}$, white arrow in the 2D images], indicative of the disordered hydrocarbon chain of the lipid. The large peak at q= 1.62 $Å^{-1}$ is the (100) diffraction of hexagonal ice (red arrows in the profile and the 2D image in Fig. 4A-(1))[26], which disappeared above 0 °C (data not shown). No ice peak was observed in the dry $EROCOC_{17+4}$ profile in Fig. 4A-(2), as expected. These results indicate that $EROCOC_{17+4}$ remained in the disordered chain state (hence no L_C phase formation) at least down to − 20 °C, over a wide range of lipid hydration values (W_{Water}) from fully hydrated 40% down to nearly 0% (w/w) water.

The adoption of the disordered chain state well below 0 °C is further supported by a differential scanning calorimetry study of the $EROCOC_{17+4}$/water system[10], which describes the effort in developing the L_C phase by cooling (ca. − 3 °C/min) the $EROCOC_{17+4}$/water system from ca. 25 to − 60 °C, followed by a 3 h isothermal incubation at − 60 °C prior to the initiation of the heating run at a rate of 0.3 °C/min. As seen in the heating thermogram of 63.0% (w/w) $EROCOC_{17+4}$ measured over a temperature range from − 40 to 15 °C (Sup. Figure 2A), only a single endothermic peak associated with melting of ice is present, indicating that $EROCOC_{17+4}$ did not adopt the L_C phase at least down to − 40 °C[10].

Let us next examine a possible phase state of the $EROCOC_{17+4}$-matrix at a cryogenic temperature. To avoid excessively rapid cooling, the $EROCOC_{17+4}$-matrix was first cooled slowly (ca. − 2 °C/min) from room temperature to − 20 °C, followed by 2–3 days of isothermal incubation prior to the incubation in liquid nitrogen (see X-ray scattering measurements section for details). We examined the diffraction profiles of twelve $EROCOC_{17+4}$-matrix specimens at − 180 °C and confirmed that all of the specimens gave disordered chain profiles, as seen in Fig. 4B-(1), where a typical diffraction image of the $EROCOC_{17+4}$-matrix (without $A_{2A}R$) at − 180 °C, measured after a one-week incubation in liquid nitrogen, is shown. It displayed a broad band profile around 4.6 Å (white arrow), indicating that the $EROCOC_{17+4}$-matrix did not adopt a crystalline L_C phase in liquid nitrogen, at least under the present experimental conditions. The four additional sharp diffractions at 3.87, 3.70, 3.44, and 2.66 Å (red arrows) are hexagonal ice diffractions[26].

The possible phase structure of the $EROCOC_{17+4}$/water system below 0 °C was inferred from the SAXS profiles of the 62.5% (w/w) $EROCOC_{17+4}$ at − 20 °C and the 63% (w/w) $EROCOC_{17+4}$ at − 60 °C. They both gave two peaks in a 2:1 ratio, 44.5 and 22.5 Å at − 20 °C and 46.8 and 23.4 Å at − 60 °C, respectively, suggesting the formation of an L_α phase with lattice constants of $\xi_{L_\alpha}(-20°C) = 44.5$ Å and $\xi_{L_\alpha}(-60°C) = 46.8$ Å, respectively. At − 180 °C, the four weak diffractions at 16.2, 12.2, 9.7, and 8.1 Å, observed in the SAXS region of Fig. 4B-(1), could also be compared with the 3rd, 4th, 5th and 6th diffractions of the L_α phase with the lattice constant of $\xi_{La}(-180°C) = 48.0$ Å. These results indicate that the $EROCOC_{17+4}$/water and the $EROCOC_{17+4}$-matrix/water systems most presumably adopted the L_α phase below 0 °C. For comparison, MO adopts the L_C phase at 1 °C (Fig. 4A-(3)), and eleven MO-matrixes subjected to the same cryo-cooling procedure displayed strong L_C diffractions at − 180 °C without exception, as shown in Sup. Figure 2.

It is therefore clear that $EROCOC_{17+4}$ is far more resistant to the adaptation of the L_C phase as compared to MO. This allowed us to readily perform the LCP-SFX data collection at a 4 °C sample temperature in a helium gas atmosphere without any L_C phase formation. Figure 4B-(2) shows a typical in situ X-ray diffraction image of the $EROCOC_{17+4}$-matrix captured during the LCP-SFX_4 °C data collection, in which the broad diffraction around 4.6 Å (white arrow) indicative of a fluid-like disordered chain state was seen, in addition to the diffraction spots from the $A_{2A}R$ crystals.

$EROCOC_{17+4}$ as a possible L_C formation-free crystal delivery medium. In LCP-SFX, the viscous media injector streams the microcrystal-dispersed LCP inside the diffraction chamber, in either vacuum or helium gas conditions. In the case of a vacuum chamber at 20 °C, the MAG-matrix must be prepared from a short chain MAG, such as 9.7 MAG or 7.9 MAG, which are less prone to L_C phase formation than MO[3,4,6]; for instance, T_K of 7.9 MAG is 6 °C[27]. For crystals that only grow in the MO-LCP, it must be doped with one of the short chain MAGs just before loading into the injector to avoid the LCP → L_C phase transition upon evaporative cooling[3,4].

Thus, the short chain 9.7 MAG and 7.9 MAG with the acyl chains of 16 carbon atoms-long serve as an L_C formation-free crystal delivery medium, whereas MO (9.9 MAG with the acyl chain of 18 carbon atoms-long, which yielded the most successful outcomes for a variety of MPs[2], Fig. 1) does not. However, the measurements without extra matrix manipulation just before loading are more favorable. Moreover, it is well known that crystal growth and quality critically rely on the hydrocarbon chain length of the matrix lipid; e.g., according to Li et al., "a chain length disparity of just one carbon (in the 14- vs 15-carbon homologues) meant either getting or not getting crystals of outer membrane sugar transporter"[28]. Thus, the short chain MAGs may not be applicable to all MPs. The lipid with the acyl chain of 18 carbon atoms-long that serves as an L_C formation-free crystal delivery medium is useful.

It is often stated rather vaguely that ICPLs remain in the fluid state at low temperatures. However, as shown in Sup. Table 1, the T_K values (the lower temperature limit of the fluid state) and the temperature range over which the LCP is stable are lipid dependent. This is also true for the maximum hydration level of LCP (W^{max}_{Water}) that determines the maximum protein buffer loading capacity of the LCP-matrix. Thus, IPCLs with these parameters favorable for the crystallization and crystal delivery medium should be explored.

$EROCOC_{17+4}$ is akin to MO, in the sense that they both contain the acyl chain of 18 carbon atoms-long (Fig. 1), and the W^{max}_{Water} value of 40% (w/w) (Sup. Table 1) is comparable to that of MO. Moreover, $EROCOC_{17+4}$ forms the stable LCP over a temperature range from ca. 0 to ca. 55 °C [10, Sup. Table 1], and remains in the fluid state at least down to − 20 °C, over a wide range of hydration levels, W_{Water} from 40% (w/w) to nearly 0% (w/w) dry state. Thus, $EROCOC_{17+4}$ represents the first lipid with the acyl chain of 18 carbon atoms-long that meets the requirements for a matrix for MPs crystallization and an L_C formation-free crystal delivery medium without extra matrix manipulations.

Concluding remarks

This study highlights the use of $EROCOC_{17+4}$ as a new matrix lipid for $A_{2A}R$ crystallization and an $A_{2A}R$ crystal delivery medium in LCP-SFX. The results are summarized as follows.

(1) The $EROCOC_{17+4}$-matrix supports the growth of X-ray diffraction quality $A_{2A}R$ crystals and serves as a crystal delivery medium in LCP-SFX.
(2) The optimum crystallization conditions for $A_{2A}R$ crystals in the $EROCOC_{17+4}$-matrix did not differ significantly from those in the MO-matrix, and the $EROCOC_{17+4}$-matrix could be manipulated by essentially the same experimental procedures as employed for the MAG-matrices. Thus, $EROCOC_{17+4}$ can readily be accommodated within the current in meso crystallography experiments.
(3) One noteworthy feature of $EROCOC_{17+4}$ and the $EROCOC_{17+4}$-matrix is the resistance to the adoption of the L_C phase. This makes it valuable for use in lower temperature crystallizations of MPs. In preliminary crystallization trials at 4 °C, we confirmed that the $EROCOC_{17+4}$-matrix yielded $A_{2A}R$ crystals that diffracted to ca. 3 Å (not optimized), suggesting that $EROCOC_{17+4}$ has potential for the in meso crystallization of thermally unstable MPs.
(4) In LCP-SFX, $EROCOC_{17+4}$ is the first lipid with the acyl chain of 18 carbon atoms-long that can serve as an L_C formation-free crystal delivery medium without extra matrix manipulations for low temperature data collection, and probably under vacuum chamber conditions as well. These features appear best suited for the lower temperature data collection of thermally unstable MP crystals, for which improved LCP-SFX diffraction data may also be expected.
(5) As $EROCOC_{17+4}$ is a member of the LCP-forming IPCL family[10–14] (Sup. Table 1), IPCLs together with MAGs will expand the reliability/efficiency of in meso crystallization and serial microcrystallography. More details about the phase behavior and physical characteristics of $EROCOC_{17+4}$ will be published elsewhere.

Methods

Expression and purification of $A_{2A}R$. $A_{2A}R$ harboring a bRIL, apocytochrome b562RIL from *Escherichia coli* (M7W, H102I, and R106L) fused in the third intracellular loop (ICL3), was prepared according to the method of Liu et al.[16]. Briefly, $A_{2A}R$ was expressed in Sf9 insect cells, using a baculovirus expression system. The $A_{2A}R$ was solubilized from the membrane fraction in 1% *n*-dodecyl-*β*-D-maltopyranoside (DDM, Anatrace) and 0.2% cholesteryl hemisuccinate (CHS, Sigma), with 4 mM theophylline (Sigma). The theophylline was substituted with 25 μM ZM241385 (Tocris and Sigma-Aldrich) on TALON cobalt-chelating resin (Clontech), in 20 mM HEPES buffer (pH 7.5) including 800 mM NaCl, 15 mM imidazole, 0.02% DDM, 0.004% CHS, and 10% glycerol, during affinity purification. The purified protein, in 20 mM HEPES buffer (pH 7.5) including 800 mM NaCl, 250 mM imidazole, 0.02% DDM, 0.004% CHS, 10% glycerol, and 25 μM ZM241385, was concentrated to 60 mg mL^{-1} (Amicon Ultra-4 100 kDa MWCO, Merck). The purity and monodispersity of the samples were assessed by analytical size exclusion chromatography (Sup. Figure 3).

Crystallization. We performed "standard" in meso crystallization trials[2,29] at 20 °C, with a 9:1 (w/w) mixture of $EROCOC_{17+4}$ and cholesterol as the crystallization matrix. As described in Fig. 1, $EROCOC_{17+4}$ is a mixture of 92% 1-*O*- and 8% 2-*O*-isomers. Typically, 9 mg of $A_{2A}R$ in buffer was homogenized with 13.5 mg $EROCOC_{17+4}$-matrix [$A_{2A}R$: $EROCOC_{17+4}$-matrix = 40:60 ratio (w/w)] by a home-made mixing device, to obtain the viscous and transparent $A_{2A}R$-LCP[30].

A 40 nL portion of the homogenized $A_{2A}R$-LCP was dispensed onto a siliconized glass plate with a 96-hole double stick sheet with a 135 μm thick spacer (Kajixx Co., Kawasaki, Japan)[30], using a home-build robotic dispenser (Hato et al., to be published). The dispensed $A_{2A}R$-LCP boluses were then covered with a glass coverslip after the addition of a series of 1 μL crystallization solutions. The 96-well glass plates were incubated at 20 °C in a RockImager 1000 (FORMULATRIX). The long axes of 10 crystals for the 30 and 32.5% PEG conditions (< 5 μm in size), 30 crystals for the 35% and 37.5% PEG conditions (~ 10 μm in size), and 50 crystals for the 40% PEG conditions (10 ~ 15 μm in size) were measured manually in bright field images (Sup. Figure 4), and the averages and standard deviations were determined. Crystal densities were also estimated by manually counting the separated and bright spots observed within a selected region of the whole (~ 40 nL) LCP bolus of cross polarized images: the whole area for the 40% PEG conditions, ~ 1/4 of the area for the 32.5–37.5% PEG conditions, and ~ 1/8 of the area for the 30% PEG conditions of corresponding LCP boluses (Sup. Figure 4). As the density values inevitably have large experimental uncertainties, they should be considered as rough estimates. The crystals for LCP-SFX were produced as described in the reference[31], except that Ito MS-GAN025 (250 μL) microsyringes were used without mixing with any other lipid before the LCP-SFX measurement. As judged from the diffraction ability, the crystals were stable between 4–25 °C for at least a few weeks.

Serial synchrotron rotation crystallography (SS-ROX). SS-ROX data were collected at 100 K at SPring-8 BL32XU[32]. After breaking the cover glass with a glass cutter[29], small crystals (~ 25 μm) in LCP were harvested with 200 μm cryo-loops (MiTeGen) and flash-cooled without additional cryo-protectant. Using a 5×5 μm^2 beam, an entire cryo-loop was scanned with 0.5° rotation and 0.45 s per image with a photon flux of 6.7×10^{11} photons/s at a wavelength of 1.0000 Å, using an EIGER X 9 M detector (DECTRIS)[20]. The experiment was performed automatically by the ZOO system[33]. Fourteen cryo-loops provided 6346 hits with more than 20 spots in an image, identified using the Cheetah program[34] adapted for EIGER, and 3701 hits were indexed using kamo.single_images_integration[20] with XDS[35]. Among the indexed images, 2100 images were selected based on the highest average $I/\sigma(I)$. Intensities were merged using kamo.merge_single_images_integrated[20] in a Monte-Carlo fashion, as in CrystFEL[36], by discarding low-partiality reflections.

Lipidic cubic phase serial femtosecond crystallography (LCP-SFX). LCP-SFX data were collected using the 20 and 4 °C samples at SACLA[37] BL3[38] EH4c (LCP-SFX_4 °C and _20 °C, Table 1). For each measurement, a ~ 25 μL $A_{2A}R$-LCP sample was transferred into a dedicated sample injector with a 75 μm ϕ nozzle. The

sample temperature was controlled by a temperature variable liquid circulator (OHM Electric Co., Ltd.) connected to the sample injector. For the data collection using the 4 °C sample, the sample injector and the circulating hose were covered with urethane and rubber jackets, respectively, to maintain the temperature and prevent condensation. The sample was injected at a rate of 0.24 μL min^{-1} into a 30 Hz X-ray laser pulse, to achieve a 30 μm inter-pulse distance at the injected sample. To achieve a smooth flow, a room temperature helium sheath gas (0.6 L min^{-1}) was applied around the injected sample, and aspirated (0.8 L min^{-1}) just below the sample. The X-ray energy was 10.1 keV (1.23 Å wavelength), the beam intensity was ~ 560 μJ per pulse, and the data were collected with a multiport CCD[39], Phase III, with improved quantum efficiency at a higher energy X-ray region around 12 keV with a thicker (300 μm) sensor. Less than 100 min were needed to obtain a complete data set with the 25 μL A_{2A}R-LCP samples (31,312 and 46,877 indexed images for 20 and 4 °C, respectively). Data collection was guided by the data processing pipeline for SACLA[40], based on Cheetah[34] and CrystFEL 0.6.2[36]. Images with 20 or more spots detected by Cheetah were considered as hits and processed by CrystFEL. DirAx 1.16[41] was used for indexing. Integrated intensities were merged by process_hkl in the CrystFEL suite, with linear scaling and the per-image resolution cutoff (the "–push-res 1.5" option).

Structural refinement. The crystal structure of MO-matrix-grown A_{2A}R (PDB ID: 4EIY) was employed as the starting model. Models were rebuilt by iterative manual modifications in COOT[42] and refinement by REFMAC5[43] in CCP4[44]. Structural figures were prepared with PyMOL (Schrödinger, L. L. C. The PyMOL Molecular Graphics System. Version 1.8). The stereochemistry of the protein structures was checked by Rampage[45], and no amino acid residues were in the disallowed region of the Ramachandran plot. Cholesterol and $EROCOC_{17+4}$ models were introduced where the shape and size of the electron density fit well. For the $EROCOC_{17+4}$ stereochemistry, (2R,3S) was applied to the erythritol moiety, and the 5,9,13,17-tetramethyloctadecanoyl moiety was modeled as the All R (5R,9R,13R) conformation, as in β-$XylOC_{16+4}$[15]. Linear hydrocarbons were modeled for elongated electron densities that could not be characterized well as a specific lipid. Polder maps[46], which exclude the bulk solvent around the individually omitted lipids E1, E2, C1, C2 and C3, were prepared with Phenix[47].

X-ray scattering measurements. The X-ray scattering measurements of dry $EROCOC_{17+4}$, 62.5% (w/w) $EROCOC_{17+4}$/water at − 20 °C, and 60% (w/w) MO/water at 1 °C were performed with a Rigaku Nano-Viewer, using Ni-filtered CuKα radiation (λ = 1.54 Å) generated by a Rigaku FR-E unit (45 kV, 45 mA) with a triple pinhole collimator (0.4 mmϕ × 0.2 mmϕ × 0.45 mmϕ). Sample-to-detector distances of 92 mm (WAXS) or 448 mm (SAXS), were calibrated by using lead stearate[48] and stearic acid[49], respectively. The sample temperature was controlled with an UT4040-PF Peltier module (Ampère, Tokyo) at − 20 ± 0.5 °C and 1 ± 0.1 °C, monitored by a Pt-100 thermoresistor (Hayashi Denko, Pt-100-A-1-M, Tokyo). The two-dimensional powder diffractions were recorded by a PILATUS100K-S detector (DECTRIS, Switzerland) and analyzed by a Rigaku 2-DP data processing system. The data collection of 63.0% (w/w) $EROCOC_{17+4}$/water at −60 °C was performed with Ni-filtered CuKα radiation (λ = 1.54 Å) from a Rigaku RU-200 X-ray generator (40 kV, 100 mA) with a double pinhole collimator (0.5 mmϕ × 0.3 mmϕ), and the sample temperature was controlled with a Mettler FP82HT temperature control-stage[10,11].

The samples (except for dry lipid) were homogenized by using a homebuilt mixing device consisting of a pair of MS-GAN025 (250 μl) microsyringes (Ito Co., Fuji, Japan) with a monolithic stainless-steel coupler[10,30]. The homogenized sample was then transferred into quartz capillaries (1.5 mm in diameter, Glass Berlin) and immediately flame sealed and glued with 5-min epoxy (Konishi Co., Ltd. Osaka). To fully develop a sub-zero degree temperature phase at − 20 °C (the L_α phase), the $EROCOC_{17+4}$ samples were first cooled (ca. − 2 °C/min) from room temperature to − 20 °C, followed by one day of isothermal incubation at − 20 °C (Medicool, Sanyo Electric Co., Ltd., Osaka) prior to the − 20 °C data collection. The − 20 °C isothermal incubation for up to three weeks did not alter the results. The MO sample was first incubated at − 20 °C to fully develop the L_C phase, and then the sample temperature was increased to 1 °C prior to the data collection at 1 °C.

The X-ray scattering profiles at − 180 °C of the $EROCOC_{17+4}$- and MO-matrixes, 60% 9:1 (w/w) $EROCOC_{17+4}$/cholesterol/water and 60% 9:1 (w/w) MO/cholesterol/water, were measured by a Rigaku FR-X unit (45 kV, 66 mA, CuKα radiation λ = 1.54 Å) with a sample to PILATUS200K detector distance of 70 mm, calibrated by using lysozyme crystals. The image data were analyzed by the Rigaku Crystal Clear data processing system.

The $EROCOC_{17+4}$- and MO-matrixes in a 200 μm cryo-loop (MiTeGen) were placed in a hermetically sealed plastic container, which contained a small amount of water at the bottom to ensure that the matrix specimens were maintained in the water saturated phase condition. To avoid excessively rapid cooling, the matrix specimens were first cooled (ca. − 2 °C/min) from room temperature to − 20 °C, followed by 2–3 days of − 20 °C isothermal incubation to fully develop a sub-zero degree temperature phase (the L_α phase), and were then incubated in liquid nitrogen. The − 180 °C measurements were performed under an evaporated liquid nitrogen flow, after 1- and 7-day incubation durations in liquid nitrogen. Both diffraction profiles were indistinguishable.

Data availability

Raw diffraction images of LCP-SFX have been deposited in the CXIDB, as entry 140. Raw diffraction images of SS-ROX_cryo are available at the Zenodo data repository (https://doi.org/10.5281/zenodo.3595784). The A_{2A}R crystal structure models of LCP-SFX_4 °C, LCP-SFX_20 °C, and SS-ROX_cryo were deposited in the Protein Data Bank, under the accession codes 6LPJ, 6LPK, and 6LPL, respectively.

Received: 15 January 2020; Accepted: 26 October 2020
Published online: 09 November 2020

References

1. Landau, E. M. & Rosenbush, J. P. A novel concept for the crystallization of membrane proteins. *Proc. Natl. Acad. Sci. USA* **93**, 14532–14535 (1996).
2. Caffrey, M. A comprehensive review of the lipid cubic phase or in meso method for crystallizing membrane and soluble proteins and complexes. *Acta Cryst. F* **71**, 3–18 (2015).
3. Weierstall, U. *et al.* Lipidic cubic phase injector facilitates membrane protein serial femtosecond crystallography. *Nat. Commun.* **5**, 3309 (2014).
4. Stauch, B. & Cherezov, V. Serial femtosecond crystallography of G protein–coupled receptors. *Annu. Rev. Biophys.* **47**, 377–397 (2018).
5. Nogly, P. *et al.* Lipidic cubic phase serial millisecond crystallography using synchrotron radiation. *IUCrJ* **1**, 168–176 (2015).
6. Caffrey, M., Lyons, J., Smyth, T. & Hart, D. J. Monoacylglycerols: The workhorse lipids for crystallizing membrane proteins in mesophases. *Curr. Top. Membr.* **63**, 83–108 (2009).
7. Qiu, H. & Caffrey, M. The phase diagram of the monoolein/water system: Metastability and equilibrium aspects. *Biomaterials* **21**, 223–234 (2000).
8. Fontell, K. Cubic phase in surfactant and surfactant-like lipid systems. *Colloid Polymer Sci.* **268**, 264–285 (1990).
9. Gruner, S. M. & Lattman, E. E. Biostructural science inspired by next-generation X-ray sources. *Annu. Rev. Biophys.* **44**, 33–51 (2015).
10. Yamashita, J., Shiono, M. & Hato, M. New lipid family that forms inverted cubic phases in equilibrium with excess water: Molecular structure–aqueous phase structure relationship for lipids with 5,9,13,17-tetramethyloctadecyl and 5,9,13,17-tetramethyloctadecanoyl chains. *J. Phys. Chem. B* **112**, 12286–12296 (2008).
11. Hato, M., Yamashita, J. & Shiono, M. Aqueous phase behavior of lipids with isoprenoid type hydrophobic chains. *J. Phys. Chem. B* **113**, 10196–10209 (2009).
12. Ishchenko, A. *et al.* Chemically stable lipids for membrane protein crystallization. *Cryst. Growth Des.* **17**, 3502–3511 (2017).
13. Hato, M., Yamashita, J., Kato, T. & Abe, Y. Aqueous phase behavior of a 1-O-phytanyl-β-D-xyloside/water system. Glycolipid-based bicontinuous cubic phases of crystallographic space groups *Pn3m* and *Ia3d*. *Langmuir* **20**, 11366–11373 (2004).
14. Fong, C. *et al.* Monodisperse nonionic isoprenoid-type hexahydrofarnesyl ethylene oxide surfactants: High throughput lyotropic liquid crystalline phase determination. *Langmuir* **27**, 2317–2326 (2011).
15. Borshchevskiy, V. *et al.* Isoprenoid-chained lipid β-XylOC_{16+4}—A novel molecule for in meso membrane protein crystallization. *J. Cryst. Growth* **312**, 3326–3330 (2010).
16. Liu, W. *et al.* Structural basis for allosteric regulation of GPCRs by sodium ions. *Science* **337**, 232–236 (2012).
17. Segala, E. *et al.* Controlling the dissociation of ligands from the adenosine A_{2A} receptor through modulation of salt bridge strength. *J. Med. Chem.* **59**, 6470–6479 (2016).
18. Weinert, T. *et al.* Serial millisecond crystallography for routine room-temperature structure determination at synchrotrons. *Nat. Commun.* **8**, 542 (2017).
19. Rucktooa, P. *et al.* Towards high throughput GPCR crystallography: In meso soaking of adenosine A_{2A} receptor crystals. *Sci. Rep.* **8**, 41 (2018).
20. Hasegawa, K. *et al.* Development of a dose-limiting data collection strategy for serial synchrotron rotation crystallography. *J. Synchrotron. Rad.* **24**, 29–41 (2017).
21. Fenalti, G. *et al.* Structural basis for bifunctional peptide recognition at human δ-opioid receptor. *Nat. Struct. Mol. Biol.* **22**, 265–268 (2015).
22. Masuda, T. *et al.* Atomic resolution structure of serine protease proteinase K at ambient temperature. *Sci. Rep.* **7**, 45604 (2017).
23. Toyoda, Y. *et al.* Ligand binding to human prostaglandin E receptor EP4 at the lipid-bilayer interface. *Nat. Chem. Biol.* **15**, 18–26 (2019).
24. Luzzati, V. & Tardieu, A. Lipid phases: Structure and structural transitions. *Ann. Rev. Phys. Chem.* **25**, 79–94 (1974).
25. Briggs, J., Chung, H. & Caffrey, M. The temperature-composition phase diagram and mesophase structure characterization of the monoolein/water system. *J. Phys. II France* **6**, 723–751 (1996).
26. Dowell, L. G., Moline, S. W. & Rinfret, A. P. A low-temperature X-ray diffraction study of ice structures formed in aqueous gelatin gels. *Biochim. Biophys. Acta* **59**, 158–167 (1962).
27. Misquitta, Y. *et al.* Rational design of lipid for membrane protein crystallization. *J. Struct. Biol.* **148**, 169–175 (2004).
28. Li, D., Lee, J. & Caffrey, M. Crystallizing membrane proteins in lipidic mesophases. A host lipid screen. *Cryst. Growth Des.* **11**, 530–537 (2011).
29. Caffrey, M. & Cherezov, V. Crystallizing membrane proteins using lipidic mesophases. *Nat. Protoc.* **4**, 706–731 (2009).
30. Hato, M., Hosaka, T., Tanabe, H., Kitsunai, T. & Yokoyama, S. A new manual dispensing system for in meso membrane protein crystallization with using a stepping motor-based dispenser. *J. Struct. Funct. Genom.* **15**, 165–171 (2014).
31. Liu, W., Ishchenko, A. & Cherezov, V. Preparation of microcrystals in lipidic cubic phase for serial femtosecond crystallography. *Nat. Protoc.* **9**, 2123–2134 (2014).
32. Hirata, K. *et al.* Achievement of protein micro-crystallography at SPring-8 beamline BL32XU. *J. Phys. Conf. Ser.* **425**, 012002 (2013).
33. Hirata, K. *et al.* ZOO: An automatic data-collection system for high-throughput structure analysis in protein microcrystallography. *Acta Cryst. D* **75**, 138–150 (2019).
34. Barty, A. *et al.* Cheetah: Software for high-throughput reduction and analysis of serial femtosecond X-ray diffraction data. *J. Appl. Cryst.* **47**, 1118–1131 (2014).
35. Kabsch, W. XDS. *Acta Cryst. D* **66**, 125–132 (2010).
36. White, T. A. *et al.* Recent developments in CrystFEL. *J. Appl. Cryst.* **49**, 680–689 (2016).
37. Ishikawa, T. *et al.* A compact X-ray free-electron laser emitting in the sub-angstrom region. *Nat. Photon.* **6**, 540–544 (2012).
38. Tono, K. *et al.* Beamline, experimental stations and photon beam diagnostics for the hard X-ray free electron laser of SACLA. *New J. Phys.* **15**, 083035 (2013).
39. Kameshima, T. *et al.* Development of an X-ray pixel detector with multi-port charge-coupled device for X-ray free-electron laser experiments. *Rev. Sci. Instrum.* **85**, 033110 (2014).
40. Nakane, T. *et al.* Data processing pipeline for serial femtosecond crystallography at SACLA. *J. Appl. Cryst.* **49**, 1035–1041 (2016).
41. Duisenberg, A. J. M. Indexing in single-crystal diffractometry with an obstinate list of reflections. *J. Appl. Cryst.* **25**, 92–96 (1992).
42. Emsley, P. & Cowtan, K. Coot: Model-building tools for molecular graphics. *Acta Cryst. D* **60**, 2126–2132 (2004).
43. Murshudov, G. N., Vagin, A. A. & Dodson, E. J. Refinement of macromolecular structures by the maximum-likelihood method. *Acta Cryst. D* **53**, 240–255 (1997).
44. Winn, M. D. *et al.* Overview of the CCP4 suite and current developments. *Acta Cryst. D* **67**, 235–242 (2011).
45. Lovell, S. C. *et al.* Structure validation by Calpha geometry: Phi, psi and Cbeta deviation. *Proteins* **50**, 437–450 (2003).
46. Liebschner, D. *et al.* Polder maps: Improving OMIT maps by excluding bulk-solvent. *Acta Cryst. D* **73**, 148–157 (2017).
47. Liebschner, D. *et al.* Macromolecular structure determination using X-rays, neutrons and electrons: Recent developments in Phenix. *Acta Cryst. D* **75**, 861–877 (2019).
48. Corbeil, M. C. & Robinet, L. X-ray powder diffraction data for selected metal soaps. *Powder Diffr.* **17**, 52–60 (2002).
49. Malta, V., Celotti, G., Zannetti, R. & Martelli, A. F. Crystal structure of C-form of stearic acid. *J. Chem. Soc.* **2**, 548–553 (1971).

Acknowledgements

We are grateful to Mariko Ikeda, Sayako Kohno, Takehiro Shinoda, Kaori Ito, Yoshiaki Kawano, Noboru Ohsawa, and Mio Inoue for their help with protein sample preparation, X-ray data collection, and expression plasmid construction. We thank Tetsuya Hori, Hiroaki Tanabe, Shinji Mori, Yoshihiro Nakamura, and Shigeyuki Yokoyama for useful discussions. We appreciate Dr. Hiroyuki Minamikawa, AIST Tsukuba, Japan, for his valuable discussion about the IPCLs. We also thank the beamline staffs of SPring-8 and SACLA for their assistance with LCP-SFX data collection. SS-ROX was performed using the Platform for Drug Discovery, Informatics, and Structural Life Science (PDIS) beam time granted to M.Sh. The XFEL experiments were conducted at BL3 of SACLA with the approval of the Japan Synchrotron Radiation Research Institute (JASRI) (Proposal Number 2017A8019). Computational analysis was performed on the SACLA HPC system and Mini-K super-computing system. This work was supported by JSPS KAKENHI Grant Number JP16K14688 to K.I. and M.H. S.I. acknowledges the Platform Project for Supporting Drug Discovery and Life Science Research (Basis for Supporting Innovative Drug Discovery and Life Science Research (BINDS)) from Japan Agency for Medical Research and Development (AMED).

Author contributions

K.I., M.H., T.K.-S., and M.Sh. designed the experiments. M.H. developed and synthesized IPCLs. K.I., M.H., Y.I.-K., T.K.-S., and M.Sh. prepared the samples. K.I., K.Y., T.H., K.H., and M.Y. performed SS-ROX at SPring-8 BL32/41XU. K.I., T.N., T.H., R.T., T.T., M.Su., O.N., K.T., E.N., and S.I. performed SFX at SACLA BL3. K.I., M.H., T.K.-S., and M.Sh. wrote the manuscript with assistance from the other authors.

Competing interests

The authors declare no competing interests.

Additional information

Supplementary information is available for this paper at https://doi.org/10.1038/s41598-020-76277-x.

Correspondence and requests for materials should be addressed to M.H. or M.S.

Reprints and permissions information is available at www.nature.com/reprints.

Publisher's note Springer Nature remains neutral with regard to jurisdictional claims in published maps and institutional affiliations.